

TECHNOLOGY DEVELOPMENT FOR EXOPLANET MISSIONS

*Technology Milestone White Paper
Vortex Coronagraph High Contrast Demonstrations*

*Gene Serabyn¹
Dimitri Mawet^{1,2}
Garreth Ruane¹
Camillo Mejia-Prada¹
Nemanja Jovanovic²*

¹Jet Propulsion Laboratory, California Institute of Technology

²California Institute of Technology

August 5, 2019



Approvals:

Released by

Gene Serabyn
Principal Investigator

Date

Approved by

Brendan Crill
Exoplanet Exploration Deputy Program Chief Technologist, JPL

Date

Nick Siegler
Exoplanet Exploration Program Chief Technologist, JPL

Date

Douglas Hudgins
Exoplanet Exploration Program Scientist, NASA HQ

Date

Table of Contents

1. Objective	3
2. The Optical Vortex Coronagraph.....	4
2.1. The Optical Vortex Coronagraph with a Clear Circular Aperture	4
2.2. Segmented-aperture Vortex Coronagraphs	6
2.3. Vortex Phase Masks	7
2.4. Past Vortex Coronagraph Performance Levels	11
2.5. The Broadband Optical Vortex Coronagraph	13
2.6. Intrinsically Broadband Optical Vortex Masks.....	13
2.7. Spectral Polarization Filtering.....	18
2.8. Pupil Apodizers for Segmented Telescopes	19
3. Milestone Definitions.....	20
3.1. Relevance for a Future Exoplanet Mission	22
4. Testbed Descriptions	23
4.1. Wavefront Control.....	23
4.2. The DST	23
4.3. The HCST	24
4.4. Differences Between Flight and Laboratory Demonstrations	26
5. Data Measurement and Analysis	28
5.1. Definitions	29
5.2. Measurement of the Star Brightness	30
5.3. Measurement of the Coronagraph Dark Hole Contrast Field	30
5.4. Milestone Demonstration Procedure	31
5.5. Milestone Data Package	32
6. Success Criteria	33
7. Schedule.....	34
8. References	35

TDEM Milestone White Paper: Vortex Coronagraph High Contrast Demonstrations

1. Objective

In support of NASA's Exoplanet Exploration Program and the ROSES Technology Development for Exoplanet Missions (TDEM), this whitepaper explains the purpose of the planned TDEM Milestones for the project entitled *Vortex Coronagraph High Contrast Demonstrations*, specifies the methodology for computing the milestone metrics, and establishes the success criteria against which the milestones will be evaluated. For consistency, the methodology for computing the milestone metrics used here is identical to the methodology set out in our previous 2016 vortex coronagraph TDEM whitepaper, *Broadband Light Rejection with the Optical Vortex Coronagraph*. Simply stated, our objective in this new work is to extend optical vortex coronagraph performance demonstrations to deeper contrasts, broader bandwidths, and segmented apertures.

The milestones described in this white paper are aimed at demonstrating improved optical vortex coronagraph performance for use in potential exoplanet space missions such as, e.g., HABEX and LUVOIR. These missions are currently considering a number of aperture types, including both unobscured off-axis monolithic and segmented apertures, and centrally-obscured segmented apertures. Addressing all conceivable aperture types is beyond the scope of this work, and we aim instead at specific improvement steps over past demonstration levels in the most relevant areas. In particular, for the case of a clear monolithic aperture, we aim at providing rejection demonstrations as deep as the best JPL high-contrast testbed, the Decadal Survey Testbed (DST), is capable of (currently a few $\times 10^{-10}$, depending on bandwidth), first for monochromatic light, and then for broadband (10% bandwidth) light. Such levels approach the intrinsic planet/star contrasts expected for terrestrial exoplanets around nearby sun-like stars.

A second aspect of our work aims at initial demonstrations of broadband (10% bandwidth) stellar rejection with an off-axis segmented aperture. As the segmented-aperture vortex coronagraph is much less mature than the monolithic aperture vortex, in this case we first aim at the 10^{-8} contrast level achievable in an open air testbed located at Caltech, and then at the 10^{-9} contrast level in JPL's in-vacuum DST.

Of course, milestones that are realistic cannot exceed the best conceivable performance of the testbed to be used. Therefore, in this white paper, we tie our specific milestones to the current best testbed performances seen recently in the JPL DST. These performance levels are in fact consistent with a simple testbed error budget that has recently been elucidated by Ruane et al. (2019). Should the intrinsic testbed performance improve beyond its present capabilities in the future, our vortex coronagraph performance levels could be improved in tandem, but given the testbed's error budget, our most realistic target contrast demonstrations are the best performance actually seen to date, and so that is the route we take here.

2. The Optical Vortex Coronagraph

2.1. The Optical Vortex Coronagraph with a Clear Circular Aperture

For any type of coronagraph, the simplest case to consider is that of a clear, monolithic, circular telescope aperture. As this case applies to both the potential Exo-C and HABEX missions, our first two project milestones are aimed at vortex coronagraph performance in the simplest case of a clear, round, monolithic telescope aperture. This is also the case that most directly probes the performance of the vortex phase mask itself, as there are no complicating factors due to, e.g., aperture edge shape, panel gaps, and apodizers.

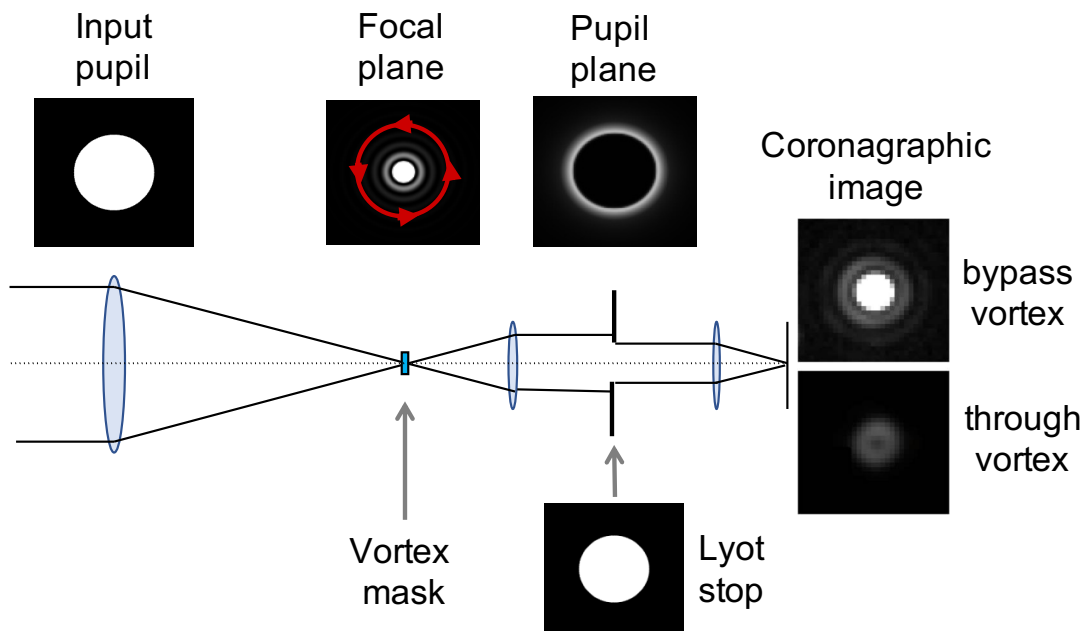


Figure 1. *Optical vortex coronagraph layout. An optical vortex phase mask in the focal plane produces a downstream pupil image in which all of the on-axis starlight appears outside of the original pupil’s image, where it is blocked by an aperture (Lyot) stop.*

Vortex coronagraphs and classical opaque-mask “Lyot” coronagraphs share the same basic optical configuration (Fig. 1). The starlight is first focused onto a phase or amplitude mask, respectively, after which a downstream optical pupil is spatially filtered with an opaque pupil stop (the “Lyot stop”). For the case of a clear, monolithic circular telescope aperture, the input pupil can be described by a field distribution, $P(r)$, given by

$$P(r) = \begin{cases} 1 & \text{for } r < R \\ 0 & \text{for } r > R, \end{cases} \quad (1)$$

where R is the input aperture radius, and r is the radial coordinate. Focusing the collimated beam after the pupil then yields the normal Airy-function focal-plane field distribution,

$$E_f(\theta) \propto \frac{J_1(kR\theta)}{kR\theta}, \quad (2)$$

where J_1 is the Bessel function of order 1, k is the wavenumber, and θ is the angular radial offset from the center of the stellar PSF. An optical vortex coronagraph then modifies the phase of this focal-plane field with an optical vortex phase mask in the focal plane (Foo et al. 2005; Mawet et al. 2005; Swartzlander 2009, Serabyn et al. 2019) that multiplies the focal-plane field by an exponential phase factor corresponding to an azimuthal phase helix, i.e., $e^{in\alpha}$, where α is the azimuthal angle, and n is an integer called the “topological charge” (the number of 2π ’s of phase in one circuit about the center). The field after the vortex phase mask is thus

$$E_f(\theta, \alpha) \propto e^{in\alpha} \frac{J_1(kR\theta)}{kR\theta}. \quad (3)$$

After passage through the vortex phase mask, the light is recollimated, typically by an off-axis paraboloid, yielding a downstream image of the pupil. Because of the applied azimuthal phase wrap and the definition of $J_n(x)$, the Bessel functions of order n , i.e.,

$$J_n(x) = \int_{-\pi}^{\pi} e^{-i(n\alpha - x\sin(\alpha))} d\alpha, \quad (4)$$

the downstream pupil plane distribution for, e.g., the case of a charge 2 vortex is proportional to (Mawet et al. 2005; Swartzlander 2009; Serabyn et al. 2019)

$$\int_0^{\infty} J_2(kr\alpha) J_1(kA\alpha) d\alpha \quad (5)$$

instead of the usual

$$\int_0^{\infty} J_0(kr\alpha) J_1(kA\alpha) d\alpha. \quad (6)$$

This change in the integrand dramatically alters the downstream pupil distribution, as all of the light originally inside the entrance pupil ends up outside the pupil. Indeed, in the ideal case, the field inside the pupil is zeroed out perfectly (e.g., Fig. 1, top right panel), with the output pupil field given in the simplest charge 2 case by

$$P(r) = \begin{cases} 0 & \text{for } r < R \\ -e^{i2\alpha} \left(\frac{R}{r}\right)^2 & \text{for } r > R. \end{cases} \quad (7)$$

In the general case of higher (even) topological charges, a uniformly zero field interior to the pupil again results, but the field exterior to the pupil acquires radial oscillations. As a result, in an ideal vortex coronagraph of any charge, the starlight can be completely blocked by a simple opaque stop (i.e., a circular aperture) matched to the pupil radius in the downstream pupil image.

The discussion to this point applies in the ideal case, i.e., for a perfect vortex phase mask and an ideal, clear, circular aperture with no wavefront aberrations. However, departures from this ideal case will result in residual light within the output pupil, leading to contrast degradation in the final focal plane image. Thus, very deep starlight rejection requires both high-quality vortex phase masks and exquisite wavefront control. Our work is thus divided along these lines as well: our TDEM team is working to develop the

requisite nearly-ideal vortex phase masks (as well as the requisite apodizers for the segmented aperture case), while the JPL high contrast facilities team is responsible for providing the requisite wavefront control procedures for generating high-contrast focal-plane dark holes in the ultimate high-contrast test facilities at JPL.

2.2. Segmented-aperture Vortex Coronagraphs

As discussed above, for a clear, circular input pupil, the optical vortex coronagraph (OVC) requires only a nearly-ideal vortex phase mask and a clear circular Lyot stop. However, achieving high rejection on obstructed and/or segmented telescopes is more involved, and generally also requires apodization of the pupil-plane light distribution. It has been shown that gray scale apodizers can theoretically compensate for unwanted diffraction from central obscurations (Mawet et al. 2013, Fogarty et al. 2017), as well as from secondary-support spiders and gaps between mirror segments (Ruane et al. 2016). Figure 2 shows an example of an apodized vortex coronagraph designed for an unobscured, off-axis, segmented telescope. The apodizer both introduces a gray scale amplitude transmission pattern that reduces diffraction from the segment gaps at angular separations $< 20 \lambda/D$, and also clips the ragged pupil edge to a circular outer boundary. Except for the throughput losses introduced by the apodizer (\sim a factor of 2 for hexagonally segmented primary mirrors), the theoretical performance of the coronagraph is practically identical to OVCs on off-axis, monolithic telescopes (Ruane et al. 2017). In fact, with the coronagraph illustrated in Fig. 2, it has been found that a 6.5 m diameter segmented off-axis telescope architecture, one of the options being considered for HabEx (Habex interim report), is expected to provide a 30% increase in the detection of Earth-like planets compared to a 4 m monolithic aperture architecture (Ruane et al. 2018). Moreover, the current “baseline” for LUVOIR B, an 8-meter off-axis segmented mirror, is an apodized vortex (LUVOIR interim report). As such, the second aspect of our TDEM project is the initial demonstration of OVC performance with a clear segmented aperture, for which the planned work includes the development of the requisite apodizers (Section 2.6).

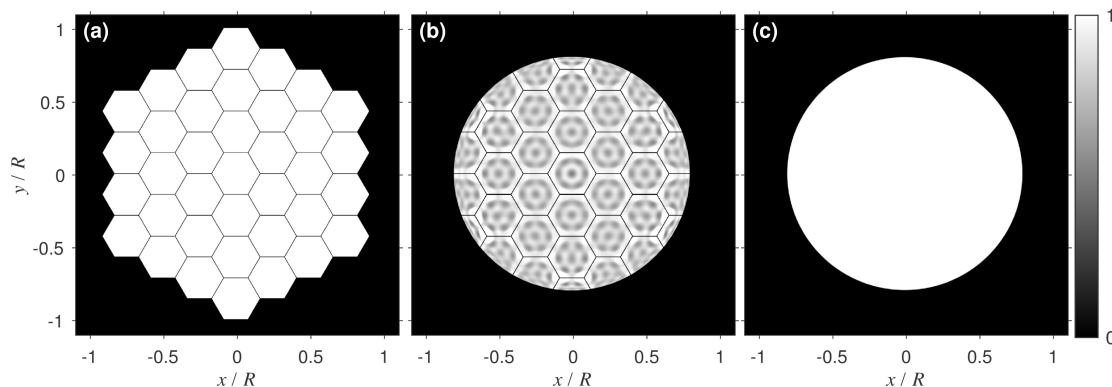


Figure 2. Apodized vortex coronagraph for an off-axis segmented telescope. (a) The non-circular segmented telescope pupil causes unwanted starlight to diffract into close-in regions of the image plane where planets are sought. The pupil apodizer (b) improves the starlight suppression by introducing a circular outer edge to diffract more starlight outside of (c) the Lyot stop. The gray scale apodizer pattern in (b) is also designed to minimize the amount of starlight diffracted into the region about the star at angles $< 20 \lambda/D$.

2.3. Vortex Phase Masks

The core optical component under test in this project is the optical vortex phase mask. The basic vortex mask pattern is an azimuthal phase ramp about a central singularity. This phase wrap can be implemented by means of longitudinal phase (the scalar vortex; Foo et al. 2005), or geometric phase (the vector vortex; Mawet et al. 2005). Several techniques for manufacturing vortex phase masks are discussed in Mawet et al. (2011a), and with different types of vortex mask possible, we note that our contrast milestones are independent of the type of vortex used to reach it; i.e., our milestones can in principle be met with *any* type of vortex phase mask. However, based on past work and current manufacturing capabilities, our baseline plan is to develop and test vector vortex phase masks made of birefringent liquid-crystal-polymer (LCP) layers. We are also exploring other less-mature technologies for manufacturing vortex phase masks under a separate APRA award, and are in contact with foreign colleagues about their work on both photonic crystal vortices (Murakami et al. 2014) and subwavelength grating vortices (Absil et al. 2016). Should any of those alternative techniques yield promising vortex masks for use at optical wavelengths, they can also be tested under our TDEM project, but such mask types remain secondary. Our baseline plan is thus to rely on LCP vector vortex masks, as these are currently the most advanced.

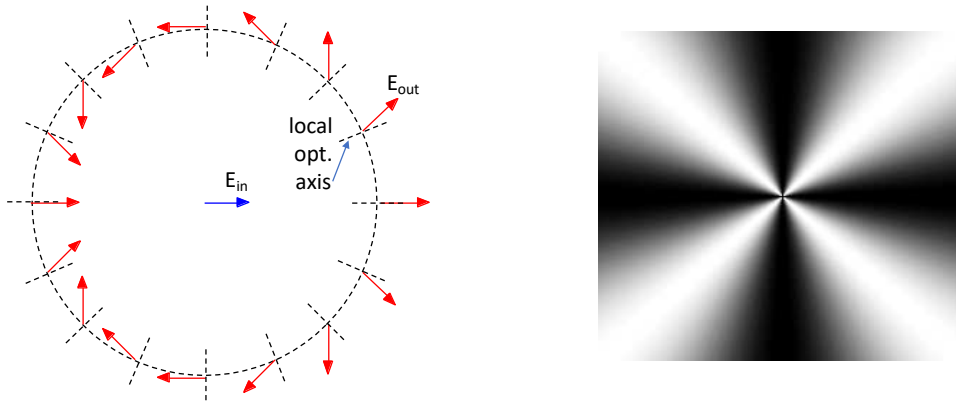


Figure 3. *Left: The optical-axis orientations (radial dashed lines) for an $n = 2$ (i.e., $q = 1$) vector vortex phase mask (for which the optical-axis orientations are everywhere radial). Such a half-wave plate structure rotates a linear input polarization vector (blue arrow) by twice the angle between the input polarization direction and the local optical axis, yielding output linear polarization directions at twice the azimuth angle (red arrows), corresponding to a charge 2 output beam. If the input vector is now imagined to be spinning, as in a circular polarization state, the red output vectors also all spin, but in the opposite direction to the input beam. As each vector is at a different orientation at a given time (as shown), a phase shift proportional to the azimuth angle results. This is the geometric phase. Right: Computation of the intensity transmitted by such a vortex mask when sandwiched between crossed polarizers (the output polarizer is vertical for the blue horizontal input state shown on the left-hand side). As the red arrows in the left-hand panel rotate twice in a circuit about the center, they are horizontal at four different azimuth angles (every $\pi/2$), yielding four dark radially-oriented transmission minima.*

A vector vortex mask is a spatially variant half-wave plate (HWP) in which the retardance between the two input polarization states is half a wave everywhere across the mask's surface, but where the local optical-axis orientation varies across the mask in such a way as to provide the desired vortex phase pattern. This geometric phase pattern arises because the electric field incident anywhere on a vector vortex mask is flipped across the local HWP axis, implying that the output field has an azimuthal rotation rate twice that of the optical axis pattern. Thus, with a vector vortex mask, an output field of topological charge n is produced by an optical-axis pattern with $n/2$ azimuthal rotations in a circuit about the center. The parameter $n/2$ that describes the mask structure is usually called q (Marrucci et al. 2006). (In contrast, for a scalar vortex phase mask the mask's physical structure and the output field pattern are both described by the same parameter, n .) As an example, Fig. 3 shows the structure and the effect of a $q = 1$ vector vortex phase mask, which has radial optical axes everywhere. Flipping a linearly polarized input field (the blue arrow in Fig. 3) across the local optical axes produces 4π of rotation of the output field in a circuit about the center, corresponding to a topological charge 2 (i.e., $n = 2$) output beam. Moreover, since HWPs reverse circular polarization states, a vector vortex phase mask also flips circular polarization states, but with an output phase that varies with azimuth, due to the azimuthally-varying optical axis orientation, as is also illustrated in Fig. 3. This “geometric” phase is the origin of the azimuthal vortex phase wrap.

To make vortex masks out of LCP layers, the layers must therefore have both precise thicknesses to provide the desired half-wave of retardance, and a lateral optical axis orientation pattern consistent with the desired “vortex” pattern. The vortex pattern is established in LCP layers by using UV alignment and polymerization to orient and lock in place the optical axes, beginning with a very thin alignment layer, after which the bulk layers are deposited and polymerized. The vertical structure of our LCP masks, shown in Figure 4 (Mawet et al. 2009), is a sandwich structure, with the LCP layers and a small central blocker (see below) made on a pair of substrates that are internally bonded together with an index-matched adhesive. Note that the final mask layers have all been polymerized, and so the layers are solid throughout the structure.

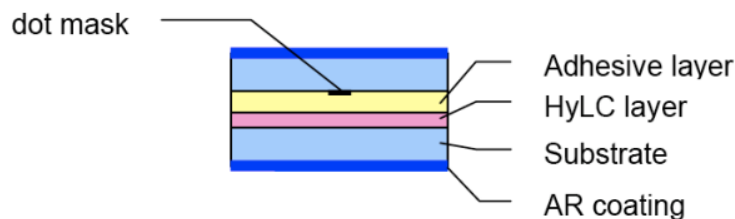


Figure 4. *Cross-section of the sandwich design for our current LCP vortex masks. The hybrid LCP (HyLC) layer is deposited on one substrate, a small opaque dot mask is placed upon another substrate, and the two are then glued together, with the dot centered on the vortex*

The q of the vortex mask's LCP structure is set by selecting the azimuthal rotation rate applied to the LCP molecules, which can be done either with a rotating laser line focus or a spatial light modulator (Serabyn et al. 2019). As vortices of higher charge are less sensitive to pointing errors and low-order aberrations (Ruane et al. 2018), the HabEx mission study is currently baselining a vortex beam of charge 6. An actual $q = 3$ mask that produces a charge 6 output beam, manufactured by Beam Engineering (Beamco), can be seen between crossed polarizers in Fig. 5.

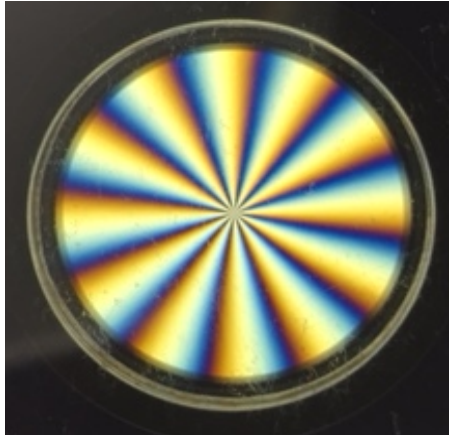


Figure 5. A $q = 3$ Beam Engineering vector vortex phase mask that yields an output beam of charge 6, seen between crossed polarizers. The diameter of the substrate is 1 inch. The phase of the vortex output beam in this case spins thrice as fast in a circuit about the center as for a charge 2 output beam, yielding 12 dark radial stripes.

In practice, the LCP spatial vortex pattern can be maintained to within a few microns of the center (Fig. 6), where the axial spin rate becomes too fast for the LCP material to follow. Any residual few-micron-sized central defect in the vortex pattern can then be covered with a small opaque mask (Fig. 7).

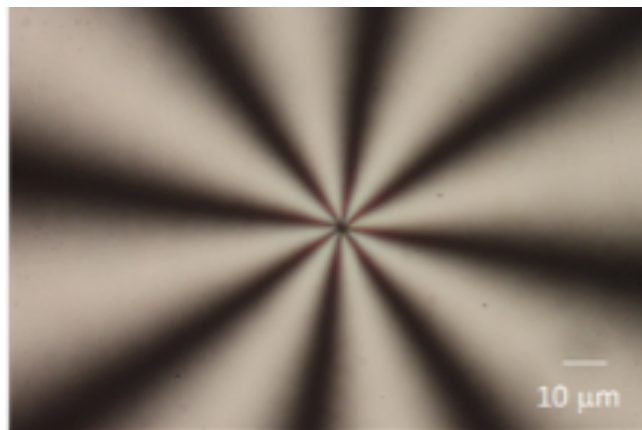


Figure 6. A $q = 2$ Beam Engineering vector vortex phase mask that produces an $n = 4$ output beam, seen between crossed polarizers. The vortex pattern is maintained down to micron scales.

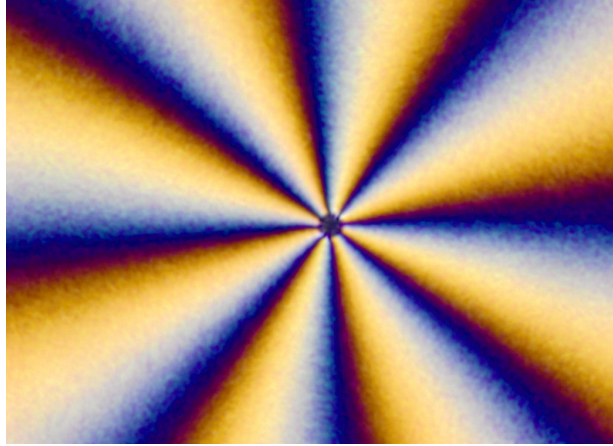


Figure 7. The central region of an $n = 4$ vortex beam produced by a mask manufactured by NC State/ImagineOptix, with a 6-8 micron diameter opaque dot mask covering the central vortex defect.

We obtain our LCP vortex masks from commercial vendors who also provide initial characterization (e.g., Figs. 5 – 7). We have recently been working mostly with Beam Engineering (Beamco), who also have a NASA SBIR award for vortex development. Initial vetting of our vortex masks prior to high-contrast testing is then carried out with our Mueller matrix imaging polarimeter at JPL, which measures both optical axis orientations (e.g., Figure 8; right-hand side) and retardance maps.

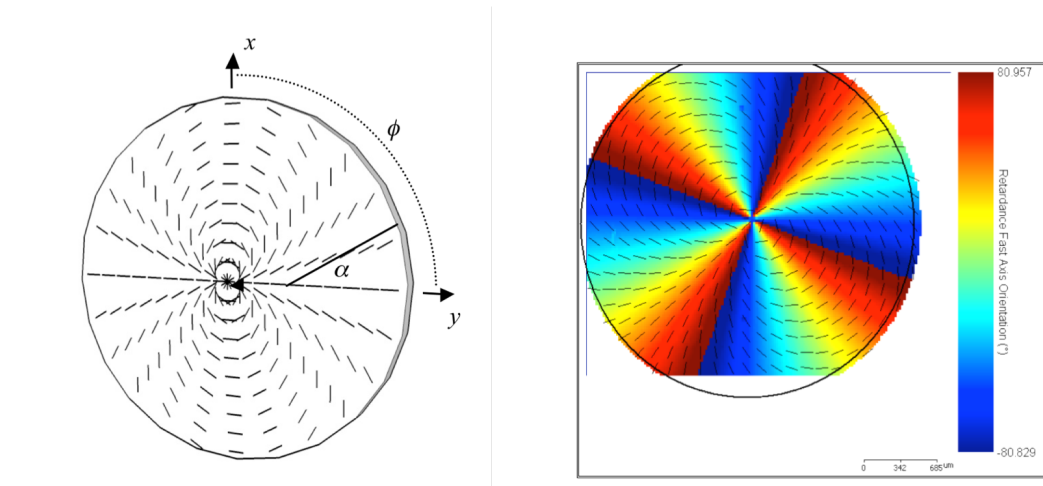


Figure 8. Left: The optical-axis orientation map for an ideal $q = 2$ vector vortex phase mask (for which the optical axes spin twice as fast as the azimuth angle) that yields an output beam of charge 4. Right: The measured optical axis orientation map (shown by both the little lines and the color scale) of a Beam Engineering $q = 2$ vortex phase mask.

2.4. Past Vortex Coronagraph Performance Levels

During our earlier TDEM awards, such vortex masks were used to reach a single-polarization, monochromatic contrast of 5×10^{-10} over a dark hole region defined by a cut-off hemisphere (Figure 9) between 3 and $8 \lambda/D$ (Serabyn et al. 2013). Our previous monochromatic milestone results are shown in Figs. 10 and 11. More recently, we have reached broadband (10% bandwidth) contrasts near 10^{-8} , as shown in Fig. 12.

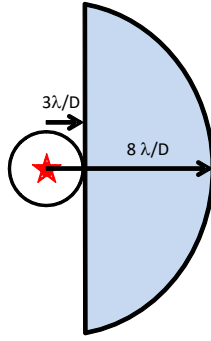


Figure 9. Target high-contrast dark field for both our previous TDEMs. As described in the text, the inner and outer edges are defined for a one-sided dark field. The location of the suppressed central star is indicated in red. The target dark hole for this demonstration would instead be from 3 to $10 \lambda/D$, to match the DST dark hole.

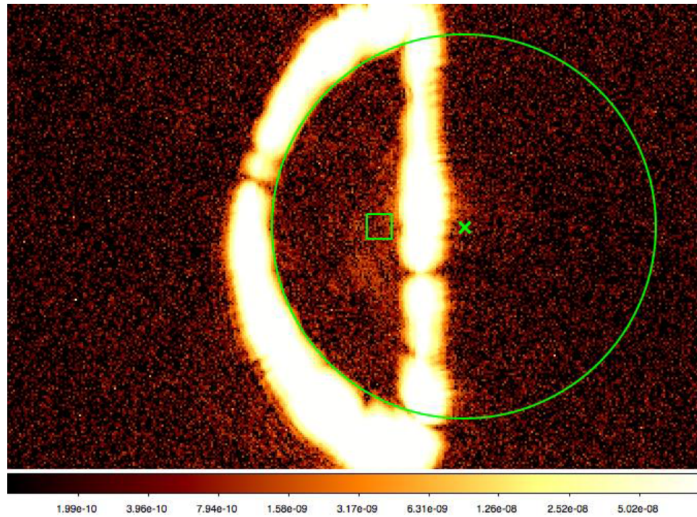


Figure 10. Final monochromatic dark hole (the interior of the reverse-D-shaped region) obtained at the end of the first milestone run of our first TDEM project. The average contrast (with contrast being the calibrated ratio of the dark hole pixel values to the value of the brightest pixel in the unattenuated star image; see Section 5) in this dark hole is 4.1×10^{-10} . The green guide lines are an $8 \lambda/D$ radius circle, a $3-4 \lambda/D$ square, and a cross marking the “star” location.

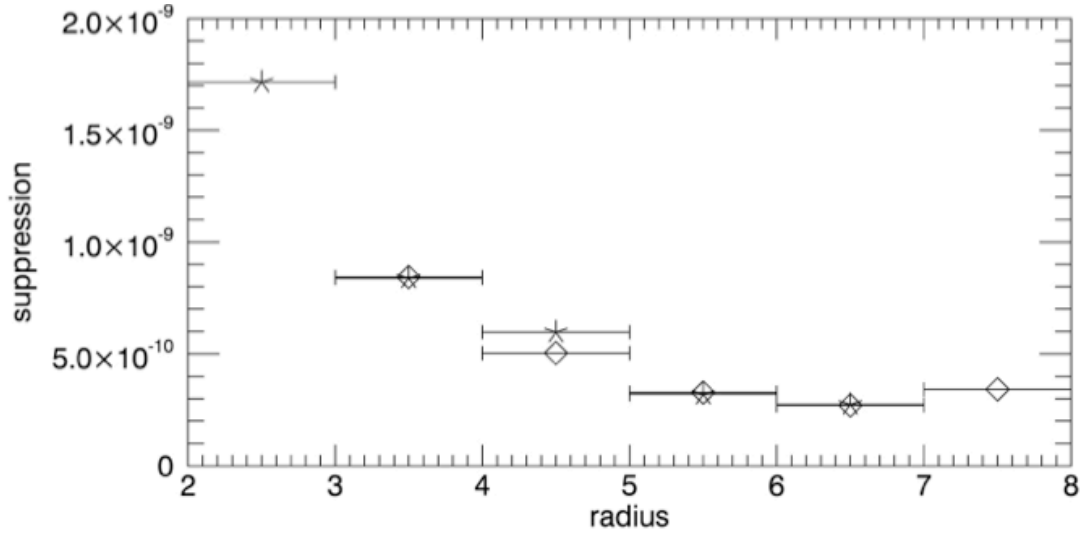


Figure 11. Radial contrast data obtained for a vortex phase mask in the HCIT, measured across dark holes extending from 3 to 8 λ/D (diamonds), and 2 to 7 λ/D (stars).

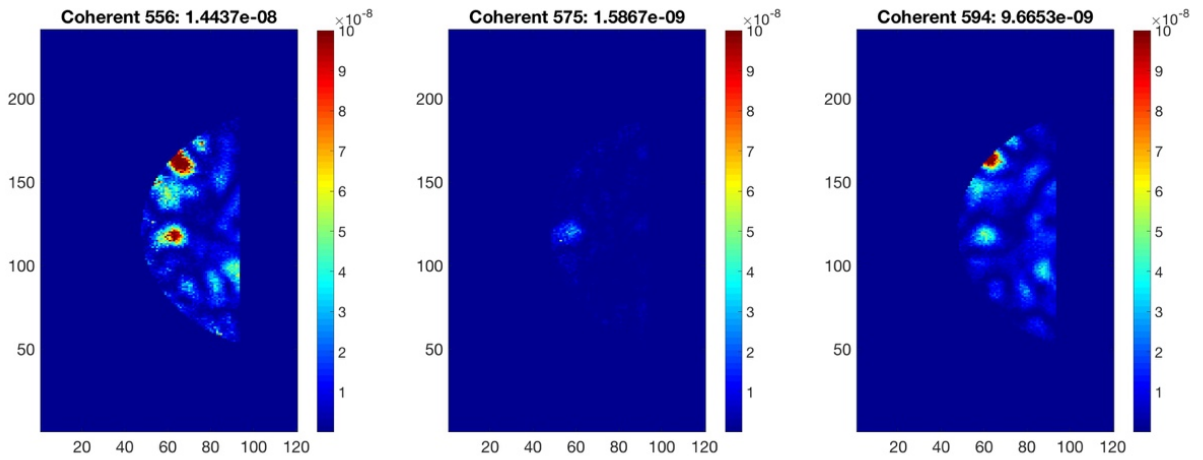


Fig. 12. Coronagraphic “dark holes” covering a simultaneous 10% passband. Each panel shows the light in a 3.33% passband, centered at 556, 575, and 594 nm. The individual average “coherent” contrasts (i.e. for light that responds to the deformable mirror) are given above each panel. The region of high wavefront correction is seen as a brighter than average C-shaped region in the right- and left-hand panels. Including all light leakage, the net contrast over the 10% bandwidth is 1.3×10^{-8} . The $F/\#$ was roughly 170.

2.5. The Broadband Optical Vortex Coronagraph

To be useful for exoplanet observations, a coronagraph must reject starlight over a broad bandwidth. As described earlier, a vector vortex mask is in essence a geometrical structure, i.e., a spatially variant HWP in which the optical axis orientation is a function of position. Such a geometric structure is of course achromatic. However, the half-wave condition on the layer thickness is not – indeed, the simplest half-wave plates only satisfy the half-wave condition at a single design wavelength, λ_o . In this case, the light at other wavelengths, λ , will not undergo perfect conversion into the opposite circular polarization state, with a leakage remaining in the original polarization state of

$$L = \frac{I_L}{I_{in}} = \left(\frac{\varepsilon}{2}\right)^2, \quad (1)$$

where ε is the wavelength-dependent phase error. Even for wavelength-independent indices of refraction the waveplate leakage is then given by

$$L = \left(\frac{\pi \lambda - \lambda_o}{2 \lambda_o}\right)^2. \quad (2)$$

Therefore, while the bulk of the post-vortex starlight emerges outside of the geometric pupil in the opposite circular polarization state, the residual stellar leakage due to wavelength-dependent phase errors remains in the original polarization state, and so can be viewed as essentially being unaffected by the vortex. This leakage thus reconstitutes a normal uniformly-illuminated pupil in a downstream, post-vortex pupil plane, ultimately producing a reduced-intensity focal-plane Airy pattern in the input polarization state.

Integrating Eqn. 2 over a passband of width $\Delta\lambda$ for a flat-spectrum source then gives a total leakage within the passband of

$$L = \frac{\pi^2}{48} \left(\frac{\Delta\lambda}{\lambda_o}\right)^2. \quad (3)$$

For example, a 10% bandwidth will have a fractional stellar leakage of $\approx 2 \times 10^{-3}$ of the input stellar flux. Such leakage will decrease with off-axis distance in the focal plane as an Airy pattern, and at $2\lambda/D$, the leakage will therefore be at approximately the 10^{-5} level. For deeper contrasts, a better means of suppressing broadband radiation is thus needed. Two techniques for passband broadening are possible: multi-layer half-wave designs that yield more intrinsically broadband vortex masks, and spectral broadening of a mask’s intrinsic rejection by means of external “spectral polarization filtering”. We plan to employ and combine both of these approaches, and so we next describe each of them in some detail

2.6. Intrinsically Broadband Optical Vortex Masks

The first approach to broader bandwidths is to achromatize the vortex HWP’s retardance. Several approaches are possible (Komanduri et al. 2012), and of these, the conceptually simplest approach would be to use the classical technique for achromatizing waveplates using multiple fixed but rotated half-wave plates (Pancharatnam 1955). A three-layer design is fairly straightforward: the three layers can all be identical, but with

the optical axes in each layer rotated with respect to the other layers by azimuthal angles of, e.g., $\sim 0^\circ$, 60° , and 0° (Fig. 13). A perfect three-layer design could in theory reach approximately the 10^{-3} radian rms level (0.06°) beyond $2 \lambda/D$, as shown in Fig. 14 (Mawet et al. 2011). Since contrast is proportional to the phase variance, three-layer devices could thus in principle provide off-axis contrasts just below 10^{-8} over a significant band, while five-layer devices could exceed the performance-level needs of terrestrial exoplanet missions.

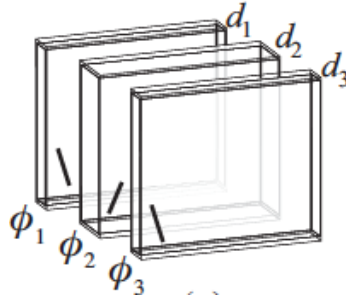


Figure 13. Classical uniform multilayer approach to broadening waveplate passbands (Komanduri et al. 2012). The successive optical axis orientations are shown.

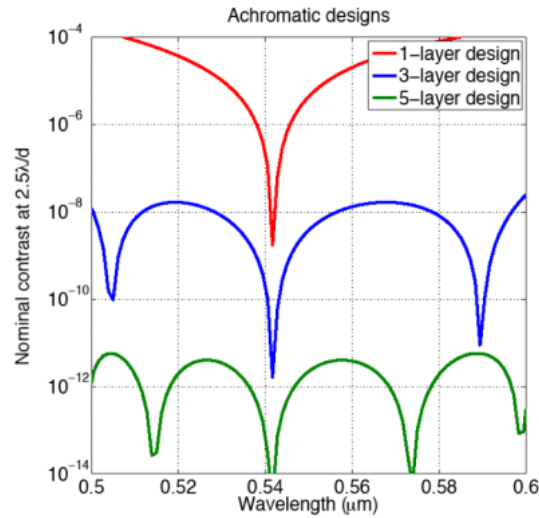


Figure 14. Predicted contrast performance outside $2 \lambda/D$ for 1, 3 and 5 layer vortex phase masks.

Fig. 15 shows the passbands achieved with such classical three-layer designs in LCP vortex phase masks recently manufactured by Beam Engineering (Serabyn et al. 2019). The plot shows the transmissions between parallel circular polarizers of a number of vortex phase plates. In this configuration, a perfect half-wave phase would result in zero transmission (Fig. 176. Although these preliminary data are not calibrated to high accuracy, one can see that the useful pass bands are quite broad ($> 20\%$). However, greater rejection depths (implying greater broadband retardance accuracies in the layers) are needed (see discussion below).

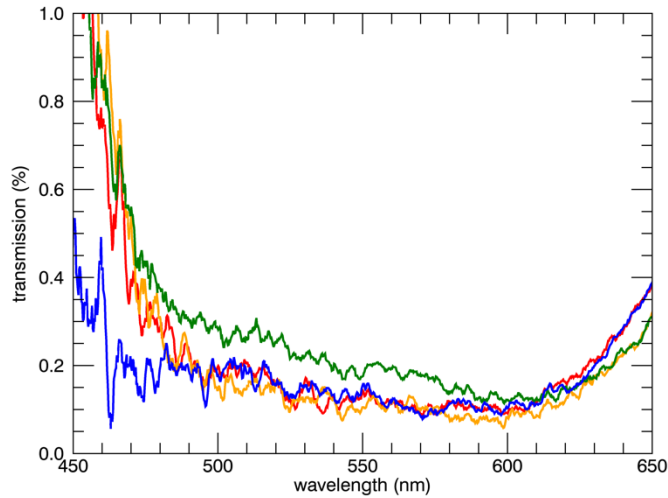


Fig. 15. Transmission between circular polarizers of a recent set of four broadband Beam Engineering vector vortex waveplates, with output beams of charge 4 (red and orange curves) and 6 (blue and green curves). These vortex masks employed a classical multi-layer HWP design with three uniform rotated layers.

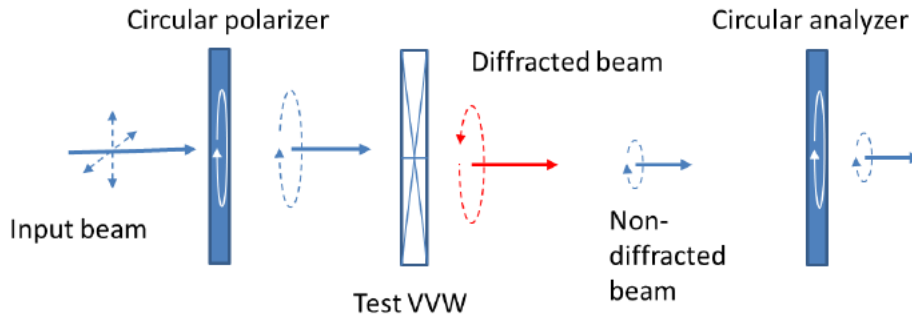


Fig. 16. Optical setup for the vortex leakage measurements.

There is a however second promising approach to the achromatization of waveplates that is unique to liquid-crystal-based devices - the use of “twisted” LCP layers, in which the optical-axis orientation within each LCP layer rotates in azimuth as one progresses vertically through the layer (Komanduri et al. 2012; Fig. 17). This approach has the advantage that successive layers can begin with the terminal optical-axis orientation of the previous LCP layer, thus eliminating optical-axis orientation discontinuities between layers. Issues such as differently-oriented layers pulling each other’s molecules out of proper alignment at layer boundaries are thus avoided, as the previous layer provides the

correct initial orientation to start laying down the next layer, whether twisted or otherwise. Note that this procedure also passes the location of the center of the vortex to the next layer, which is not possible with rotated uniform layers (which require more stringent external alignment controls between layers). However, while twisted layers may be able to solve two problems at once, they are more difficult to manufacture, as not only does the layer thickness need to be carefully controlled, but also the molecular twist rate within the layers.

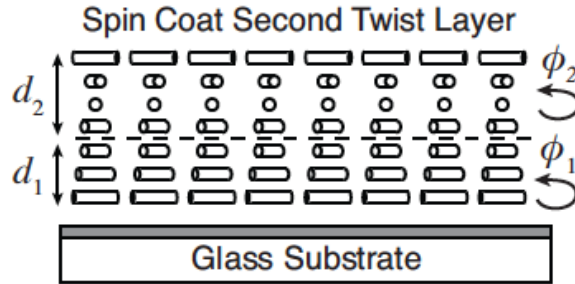


Figure 17. Internal rotation of twisted LCP layers (Komanduri et al. 2012)

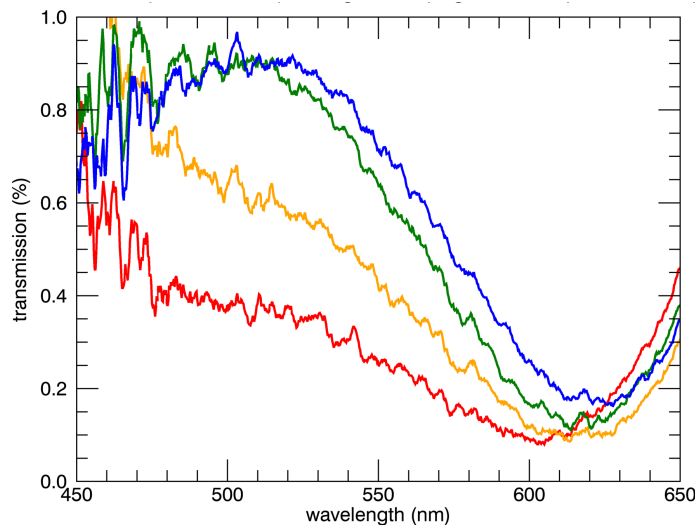


Figure 18. Transmission between circular polarizers of a recent set of four broadband Beam Engineering vector vortex waveplates, with output beams of charge 4 (red and orange curves) and 6 (blue and green curves). These vortex masks employed a “twisted-uniform-twisted” three-layer HWP design.

Both of our current potential vortex vendors, Beam Engineering and ImagineOptix, have experience with these approaches; indeed, one of them invented the twisted layer approach (Komanduri et al. 2012). Fig. 18 shows some initial results already obtained with broadband vortex masks manufactured with the twisted multi-layer approach by Beam Engineering. Evidently this approach also yields wide bandwidths in theory, but performance improvements are needed, and so far the triple-uniform-layer is superior. Indeed, a wide variety of differently layered structures are possible (Roberts et al. 2019), including twist-inverse-twist, triple-twisted-layers, twisted-uniform-twisted (TUT), etc., and we have recently carried out a theoretical error analysis (Roberts et al. 2019) on a variety of different mask types (e.g., Fig. 19). The next goal is to compare these model

predictions to real masks manufactured using the latest set of upgrades, to determine which types of mask are easier to manufacture to the required tolerances in practice, and to test the resultant masks in a high contrast coronagraph at JPL.

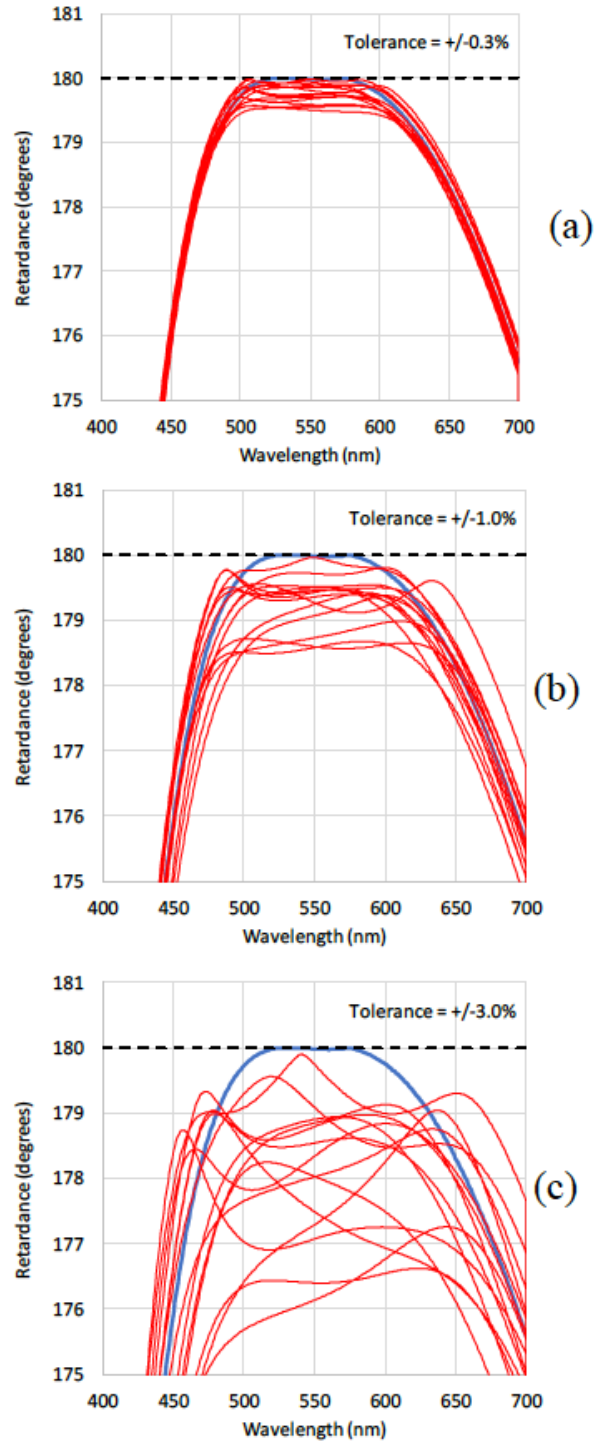


Figure 19. Tolerance analysis for twisted-uniform-twisted (TUT) three-layer design. Values of $L\Delta n$ and twist angles varied randomly by (a) $\pm 0.3\%$; (b) $\pm 1\%$; (c) $\pm 3\%$.

2.7. Spectral Polarization Filtering

An independent way to obtain more broadband vortex performance is to use polarization filtering to reduce the spectral leakage. The reason for this is that a circular polarizer can be used to reject the residual starlight remaining inside the pupil in the original circular polarization state (Fig. 20). This necessitates splitting the two circular polarization states prior to the vortex. The net starlight rejection thus relies on the combination of a Lyot stop to remove the bulk of the direct starlight that lies outside of the post-vortex pupil, and polarization filtering to remove the chromatic leakage that lies inside the pupil, as illustrated in Fig. 20.

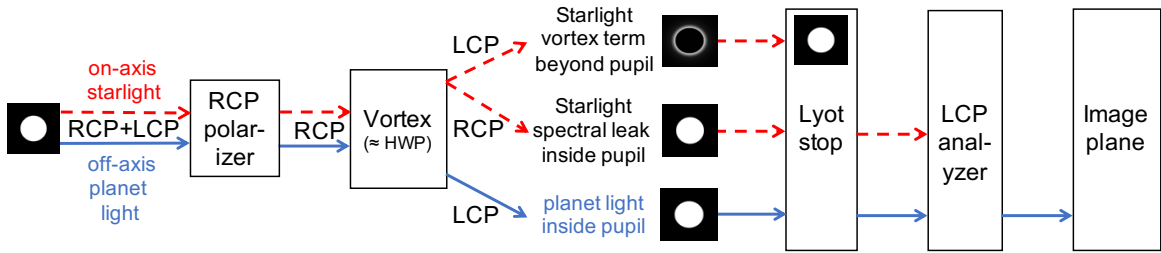


Figure 20. *Spectral polarization filtering. The starlight is shown in red, and the planet light in blue. RCP and LCP stand for right circular polarization and left circular polarization, respectively. The starlight outside the pupil is rejected by a Lyot stop (aperture), while the spectral starlight leakage inside the pupil is rejected by a circular polarizer.*

In this approach, the final rejection will then also be determined by the accuracies of the circular polarizers, as any deviations from a broadband $\pi/4$ phase shift will lead to similar chromatic leakages, making achromatic quarter wave plates essential for deep starlight rejection as well. The input and output circular polarizers together constitute a sequence made up of a linear polarizer (P) and a quarter wave plate (Q), followed by a second quarter wave plate and a final linear polarizer [or in short, a PQQP sequence], into the center of which the vortex mask is inserted for high-contrast observations. From Eqn. 1, individual waveplate phase errors corresponding to a degree of phase yield roughly 10^{-4} rejection, implying that if the vortex and the PQQP assembly both have degree-level phase accuracies, off-axis rejection levels below 10^{-10} should be possible at off-axis distances beyond $2F\lambda$ (assuming a factor of 10^{-2} suppression for being that far off the stellar position), because the filtering steps are multiplicative. (Of course, this also assumes adequate wavefront correction, and the adequate suppression of other leakage sources, such as Fresnel reflections from optical interfaces.) A tradeoff is thus possible between the phase accuracies of the quarter wave plates and the vortex phase mask, but it is clear that high-quality vortex phase masks and quarter-wave plates are both necessary to reach high contrast.

2.8. Pupil Apodizers for Segmented Telescopes

For the apodizers needed for the segmented aperture case, we will focus on demonstrating apodizers implemented using patterned microdots on glass substrates (Mawet et al. 2013, Bottom et al. 2016). In preliminary studies, we had a prototype of the apodizer fabricated by Opto-Line International (see Fig. 21). The desired gray scale pattern was approximated by exposing the anti-reflective-coated glass substrate underneath a 400 nm thick layer of gold in $10 \times 10 \mu\text{m}$ square regions of varying density. Measurements of complex reflectance of the sample showed good agreement with the desired gray scale pattern and <1 nm rms of mid-spatial frequency aberration (Zhang et al. 2018). Milestones 2a and 2b will demonstrate that such masks may be used to achieve contrasts of 10^{-8} (initially; at Caltech) and then 10^{-9} (in the second phase at JPL) for 10% bandwidth light.

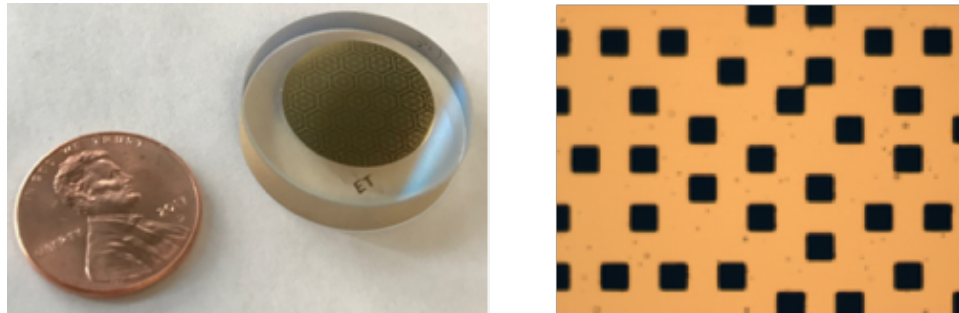


Figure 21. *Left: Apodizer fabricated for an off-axis segmented telescope. The gray scale apodization function is achieved by patterning $10 \mu\text{m}$ squares where the anti-reflective substrate is exposed. The coin is shown for scale. (right) Microscope image of the microdot pattern. The black squares are $10 \mu\text{m} \times 10 \mu\text{m}$*

3. Milestone Definitions

TDEM Technology Milestones are intended to document progress in the development of key technologies for a space-based mission that would detect and characterize exoplanets, such as Exo-C, Habex and LUVOIR, thereby gauging the mission concept’s readiness to proceed from pre-Phase A to Phase A. This TDEM’s milestones address starlight suppression with the optical vortex coronagraph, its ultimate objectives being the validation of the vortex focal-plane mask with broadband light, for both monolithic and segmented clear, off-axis apertures. Our milestones thus focus on the validation of key TDEM technology components such as the vortex mask and the associated pupil apodizer. Success is defined in terms of quantified performance demonstrations employing these key technologies. These demonstrations will need to be carried out in state-of-the-art high-contrast testbeds that are maximally isolated from extraneous environmental factors such as vibration, pointing and temperature fluctuations. Our milestones are divided into two pairs, the first pair being concerned with clear, monolithic apertures, and the second pair with clear, segmented apertures.

Before presenting our specific milestones, one must of course address the potential best contrast performance of the testbed itself. An error budget for the current performance of JPL’s Decadal Survey Testbed (DST) is given in Ruane et al. (2019), and is reproduced here as Table 1. Based on these error budget terms, which give a current best monochromatic testbed contrast of 2×10^{-10} , and a current best broadband (10% BW) testbed contrast of 4×10^{-10} , limited in part by the vertical resolution of the testbed deformable mirror (DM). Allowing also for a margin of 1×10^{-10} in both cases, realistic contrast milestones that are directly tied to the best current testbed performances are 3×10^{-10} (monochromatic) and 5×10^{-10} (10% BW). These milestones are stated formally in the following paragraphs. We would of course prefer to aim at even deeper contrasts, i.e., 1×10^{-10} , and should the DST testbed’s performance be upgraded at some point to allow that level to be reached, our milestones could be re-evaluated at that time.

	Error source	Contrast contribution
Testbed hardware	DM electronics	$\sim 1 \times 10^{-10}$
	Other incoherent background	$\sim 1 \times 10^{-10}$
Coronagraph design	FPM substrate ghost	$\sim 1 \times 10^{-10}$
	Coronagraph chromaticity	$\sim 1 \times 10^{-10}$
Total:		4×10^{-10}

Table 1. Current DST error budget estimate (from Ruane et al. 2019).

List of vortex milestones:

1. To validate vortex performance in the case of unobscured, off-axis, monolithic input apertures, we plan the following pair of milestones:

Milestone 1a: Monochromatic Starlight Suppression with Optical Vortex Phase Masks, for a clear monolithic input pupil

Using optical vortex phase masks and a clear monolithic input pupil, demonstrate a calibrated average coronagraph contrast of 3×10^{-10} (i.e., as deep as the DST currently allows) for at least one polarization state, over angular separations of $3 \lambda/D$ to $10 \lambda/D$ from a point source image, for monochromatic light anywhere in the wavelength range 300–1000 nm.

Milestone 1b: Broadband Starlight Suppression with Optical Vortex Phase Masks, for a clear monolithic input pupil

Using optical vortex phase masks and a clear monolithic input pupil, demonstrate a calibrated average coronagraph contrast of 5×10^{-10} (i.e., as deep as the DST currently allows) for at least one polarization state, over angular separations of $3 \lambda/D$ to $10 \lambda/D$ from a point source image, for a 10% bandwidth of light anywhere in the wavelength range 300–1000 nm.

The “angular separations” are defined in terms of the wavelength λ and the diameter D of the aperture stop on the deformable mirror (DM), which is the pupil-defining element of the laboratory coronagraph. Our performance metric is the average contrast in the dark hole region specified in the milestones. Contrast is defined (section 5) for any point in the field as the calibrated ratio of the residual light level at that location to the light level at the peak pixel of the point source point spread function in the absence of a coronagraphic mask.

2. To validate vortex performance in the case of an unobscured, segmented input aperture, we plan the following pair of milestones:

Milestone 2a: Broadband Starlight Suppression with Optical Vortex Phase Masks, for an unobscured, off-axis segmented input pupil

Using optical vortex phase masks and an unobscured off-axis segmented input pupil, demonstrate a calibrated average coronagraph contrast of 1×10^{-8} or better for at least one polarization state, over angular separations of $3 \lambda/D$ to $10 \lambda/D$ from a point source image, for any 10% bandwidth of light in the wavelength range 300–1000 nm.

Milestone 2b: Broadband Starlight Suppression with Optical Vortex Phase Masks, for an unobscured, off-axis segmented input pupil

Using optical vortex phase masks and an unobscured off-axis segmented input pupil, demonstrate a calibrated average coronagraph contrast of 1×10^{-9} or better for at least one polarization state, over angular separations of $3 \lambda/D$ to $10 \lambda/D$ from a point source image, for any 10% bandwidth of light in the wavelength range 300–1000 nm.

3.1. Relevance for a Future Exoplanet Mission

Development of vortex technology is intended to advance the readiness of mission concepts for the coronagraphic imaging and spectroscopy of exoplanetary systems. The small inner working angle (IWA) capability of the vortex coronagraph allows consideration of a range of mission sizes, from probe-scale (Exo-C) to many meter diameter flagship-scale missions (Habex and LUVOIR). Terrestrial exoplanet analogs with an albedo of 0.3 occur at a contrast of $\approx 2 \times 10^{-10}$, motivating our clear-aperture milestone demonstration levels, which are as close to this level as possible with the DST. As segmented-aperture coronagraphs are much less mature, our segmented aperture coronagraph milestones are at the more modest 10^{-8} and 10^{-9} levels.

Exoplanet imaging missions use a deformable mirror to form a high contrast “dark hole” or “dark field” over a working angle spanning $\sim n_i \lambda/D$ to $n_o \lambda/2D$, where n_i sets the IWA, as defined by the science requirements, the intrinsic capabilities of the coronagraph, and the wavefront and pointing control capabilities of the mission, and n_o sets the outer working angle (OWA). The OWA is defined by the highest spatial frequency controlled by the DM aperture selected, and n_o is typically somewhat smaller than $n_{DM}/2$, where n_{DM} is the number of actuators across the deformable mirror, in order to allow for finite gradients in the transition from the dark hole region to the outer bright region.

Our previous vortex milestone dark holes specified IWAs of $3\lambda/D$, and WFIRST is also aiming at a $3\lambda/D$ IWA for its coronagraph. Somewhat smaller IWA values are theoretically possible with the vortex coronagraph, but as our main goals here are contrast and bandwidth performance, we use $IWA = 3\lambda/D$ here as well. For the OWA, we take the OWA of the demonstrated Decadal Survey Testbed (DST) dark hole, $10\lambda/D$ (Ruane et al. 2019). Both the 48 x 48 element Xinetics DM and the 50 x 50 element Boston Micromachines DM can reach this OWA, as the theoretical maximum OWAs for these DMs are $24\lambda/D$ and $25\lambda/D$, respectively.

The OWA also impacts the collimated beam diameter, and so could impact the diameters of any polarization or waveplate components needed in a single-polarization vortex coronagraph. However, this effect is quite manageable: in the testbeds, the initial polarizer and quarter wave plate are to be inserted prior to the source pinhole, where the beam diameter is small, and the second quarter-wave plate and polarizer will be inserted into the collimated beam downstream of the Lyot stop, where the beam diameter is also reduced relative to its diameter at the DM. Standard 1-inch polarizer and quarter-wave plate optics should thus serve in the testbed.

4. Testbed Descriptions

As described earlier, our two pairs of milestones consist of a pair involving monolithic apertures and a pair involving segmented apertures. These milestone pairs can therefore initially be pursued independently on different high-contrast testbeds. In particular, the segmented-aperture work will begin on Caltech’s High-Contrast Segmented Testbed (HCST), while the monolithic-aperture work will be carried out on JPL’s Decadal Survey Testbed (DST). However, to reach our ultimate segmented-aperture milestones, our segmented-aperture work will also need to transition to the DST once that testbed is equipped with a segmented-aperture simulator. We now describe both of the testbeds to be used in our work, including their demonstrated capabilities. The two testbeds needed for our TDEM work are:

DST: Our monolithic aperture contrast milestones clearly require the best testbed available, which at present is the DST, a vacuum testbed at JPL that has demonstrated a best 10% BW contrast of 4.5×10^{-10} (Ruane et al. 2019). Once outfitted with a segmented-aperture capability, the DST will also be used for our ultimate segmented-aperture contrast tests.

HCST: This open-air Caltech testbed will be the initial venue for our segmented-aperture high-contrast tests, until the 10^{-8} contrast level is reached. Thereafter, and once the DST is outfitted with a segmented-aperture capability, our segmented-aperture tests will transition to the DST.

4.1. Wavefront Control

Our milestone demonstrations will rely on a wavefront sensing and correction process that has been used in several previous JPL high-contrast demonstrations, including our earlier vortex work. A variant of the “electric field conjugation method” (EFC) (Give’on et al. 2007), is used and iterated as necessary. For a given wavelength, and starting with a nominally flat surface figure setting on the DM, one: (a) takes a set of contrast field images with the initial DM setting; (b) takes images for each of four “probe” DM settings (consisting of small deterministic surface figure deviations from the initial DM setting), (c) uses these data to compute the complex electric field in the target dark field region; and then (d) calculates and applies a new DM setting that will reduce the energy over the dark field, thus establishing a new “initial DM setting” in preparation for the next iteration, which is a loop back to step (a). A typical integration time for an individual image is expected to be several seconds, and a complete wavefront sensing and control cycle, including CCD readout overheads, data handling and computations, is expected to take several minutes.

4.2. The DST

The DST optical system (Fig. 22) resides in a vacuum chamber that can be evacuated to ~ 10 milliTorr. For vortex work, we will modify the standard DST configuration with the addition of two circular polarizers (each of which is composed of a linear polarizer and a

quarter-wave retarder). The first circular polarizer will reside inside the light source assembly to generate a single pure circular polarization state, and the second will reside either just after the Lyot stop or the field stop to select the desired output polarization state. All four elements will need to be accurately rotatable, as well as individually removable from the beam, while the DST chamber is under vacuum.

As of March 2019, the DST team achieved a mean raw contrast of 4×10^{-10} averaged over angular separations $3-9 \lambda/D$ with a bandwidth of $\Delta\lambda/\lambda=0.1$ about $\lambda=550\text{nm}$ using a Lyot coronagraph in a single polarization. With the same setup in monochromatic light, the deepest raw contrast was 2×10^{-10} with the same dark hole region.

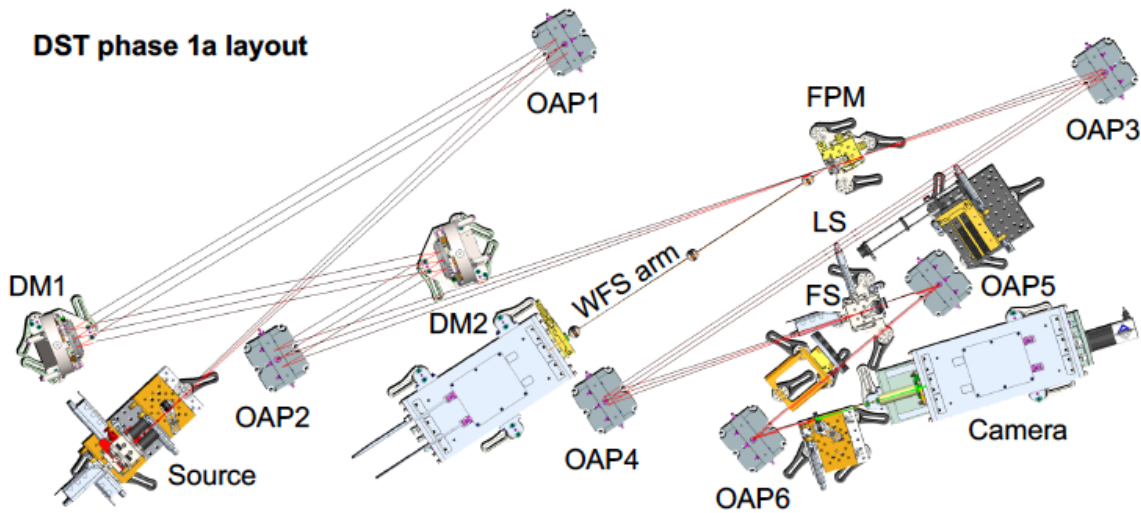


Figure 22. *Optical layout of the DST. OAP = off-axis paraboloidal mirror. DM = deformable mirror. FPM = focal plane mask. LS = Lyot stop. FS = field stop.*

4.3. The HCST

The High Contrast High-Resolution Spectroscopy Testbed for Segmented Telescopes (HCST) at the Exoplanet Technology Laboratory at Caltech is optimized to fast track the development of high contrast imaging and spectroscopy technologies for future ground and space-based telescopes (e.g. TMT, HabEx, LUVOIR). The HCST is equipped with a supercontinuum white-light source connected to an NKT VARIA tunable filter, which allows wavelength scanning over arbitrary bandwidths in the visible. The wavefront correction is performed with a Boston Micromachines kilo-DM, a deformable mirror with 32×32 actuators. The coronagraph system consists of a 3-plane coronagraph with an apodizer, focal plane mask, and a Lyot stop. The focal plane mask for this work will be a vortex phase mask. The layout of HCST is shown in Figure 23.

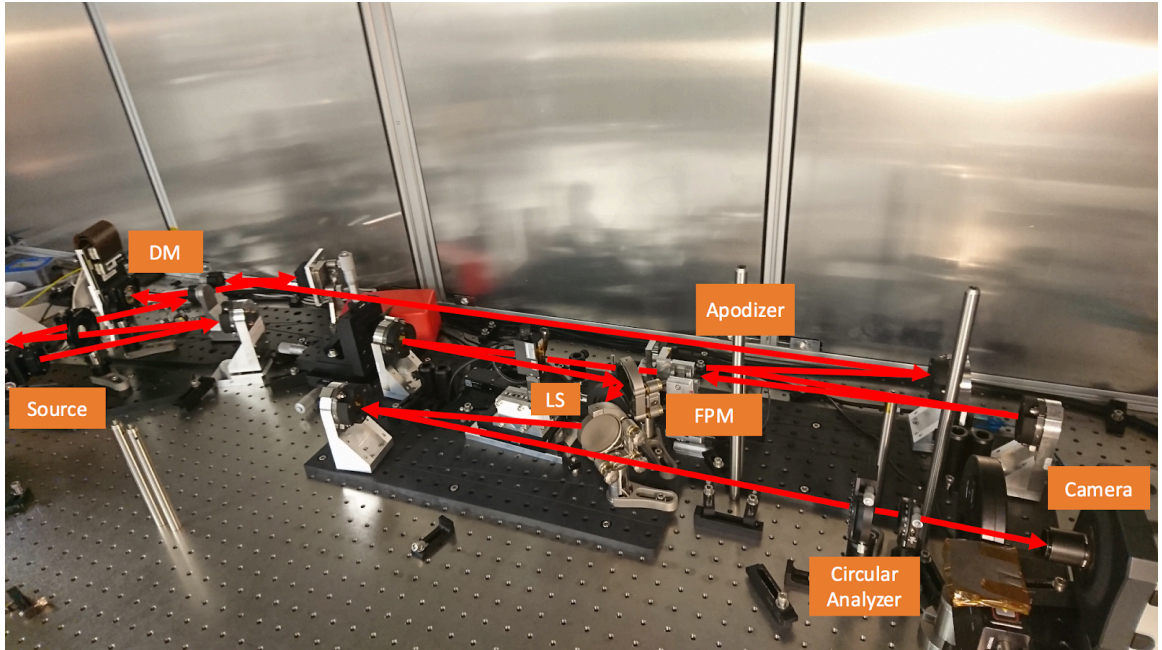


Figure 23. *Picture of the HCST at Caltech.*

HCST's wavefront correction capabilities were recently tested in monochromatic light at 775 nm, for which a dark hole with an average raw contrast of 1×10^{-8} (Fig. 24) was achieved using the EFC algorithm (Give'on 2009) in the FALCO wavefront sensing and control package (Riggs et al., 2018). FALCO enables fast computations for the optical system Jacobians, which, combined with the relatively fast integration times, allows one to achieve $\sim 10^{-8}$ contrasts after ~ 20 iterations, in under an hour.

Fig. 25 shows the result over the same dark hole with 10% broadband light centered at 775 nm, controlling 3 wavelengths in a 10% passband with FALCO. The best raw contrast level currently achieved in a 10% BW is $\sim 5 \times 10^{-8}$. On-going work on the bench is aimed at tackling the limitations of the HCST to (1) improve the image sharpening and phase retrieval algorithms, (2) improve the optical system model on which EFC relies by implementing a system identification algorithm as done by Sun et al., 2019, and (3) reduce polarization leakage in the system with a new high precision rotation stages for the circular analyzer.

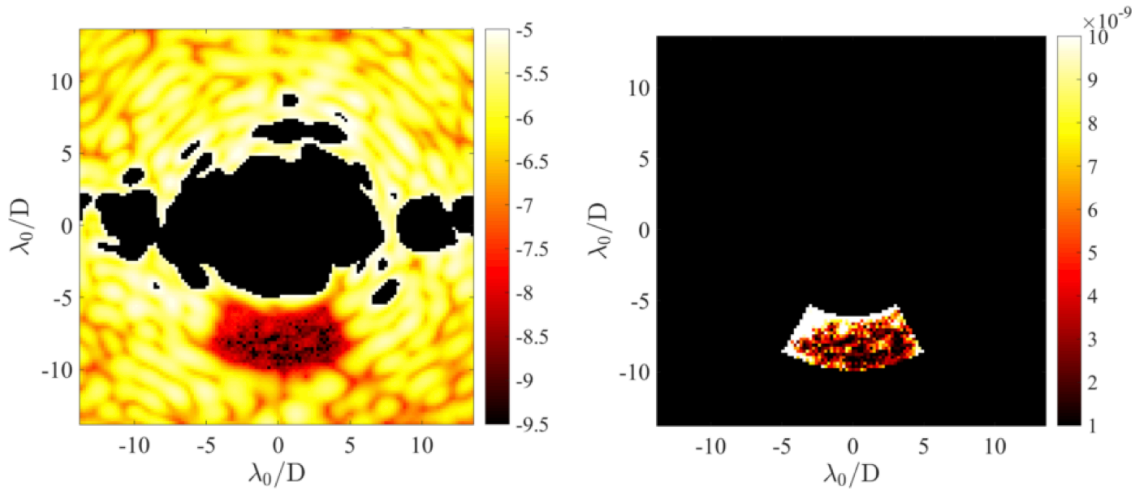


Figure 24. *Monochromatic dark hole in the HCST at Caltech.*

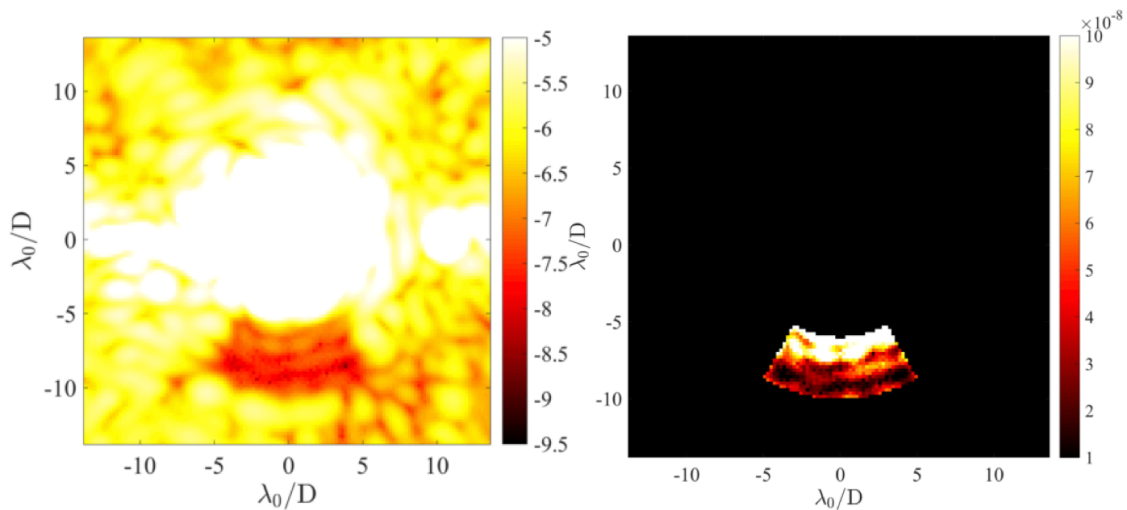


Figure 25. *Broadband (10%) dark hole in the HCST at Caltech.*

4.4. Differences Between Flight and Laboratory Demonstrations

Although the vortex coronagraph layouts in the laboratory DST and HCST are conceptually the same as is being proposed for future flight implementations on exoplanet space missions such as Habex, LUVOIR, there are several differences:

Light intensity: In a space coronagraph, the spectrum of light illuminating the coronagraph would closely resemble black body radiation, while for these milestones, the source will be a broadband supercontinuum source filtered to the desired of bandwidth. This source provides a photon flux that is comparable to or somewhat brighter than the target stars to

be observed. The goal of these milestones is to demonstrate the contrast that can be achieved with a vortex coronagraph, independent of the source intensity. A bright source is a convenience that does not compromise the integrity of the demonstration, as it affects only the integration times.

Light spatial uniformity: Unlike the light incident on a telescope from a target star, the light intensity in the testbeds is not uniform across the pupil. Typically, the light intensity drops center-to-edge by a few percent, due to the diffraction pattern from the small source pinhole. This small non-uniformity is expected to have a negligible effect on the final contrast if it is accounted for in the wavefront control algorithm, and a small but below-requirement loss of contrast if it is ignored in the control algorithm.

Number of polarization states: The laboratory layout will allow us to probe the need to separate polarization states to reach high contrast. Our input circular polarizer will be located upstream of the pinhole, which is not where it would be in a flight system, where it would need to be located in a more spatially extended beam. Our goal is therefore to show that a dark hole of the requisite depth can be generated in this more ideal single-polarization situation.

Number of deformable mirrors: Both in the laboratory and in space, highest contrasts call for two DMs in the optical system, in order to allow for the control of both phase and amplitude errors in the complex wavefront over one half of the coronagraph field described. A pair of DMs may also be used in series to generate a full two-sided dark hole, and can provide better broadband control through the use of the Talbot effect. The DST makes use of a pair of DMs, as is planned for future high-contrast space missions, and is thus essential to meeting our contrast requirements.

Spacecraft dynamics: A control system is required in flight to stabilize the light path against motions of the spacecraft. The dominant effects of spacecraft dynamics are jitter of the star image on the coronagraphic focal plane mask and beam walk in the optics upstream of the focal plane mask. For a specific example, the ACCESS analysis (Trauger et al. 2010) showed that for fourth-order coronagraphs (including Lyot, vortex, and pupil mapping coronagraphs) with an inner working angle of $3\lambda/D$, rms pointing errors need to be $< \pm 0.03 \lambda/D$ to limit the contrast degradation to $< 2 \times 10^{-10}$. The concept models have shown that the required pointing stability can be achieved in space with current high Technology Readiness Level (TRL) systems. In the DST, this would correspond to an ability to center the vortex mask on the “star” within about $2.5 \mu\text{m}$, or about 0.2 pixel when projected to the CCD focal plane.

The milestone demonstration requires passive stability of the testbed, which is thus untraceable to spacecraft dynamics. In practice, the DST may exhibit alignment drifts that are larger than expected in the space environment. If so, we will rely on favorable periods of thermal and mechanical stability of the DST.

5. Data Measurement and Analysis

A contrast measurement is a measurement of the intensity of the residual light (speckles, background, etc.) within the dark field, relative to the peak intensity of an image of the source. There will of course be a distribution of intensities across the dark hole, from which the average contrast and its statistical confidence level will be calculated. The milestone objective is to demonstrate with high confidence ($\geq 90\%$) that the true contrast in the dark field, as estimated from our measurements in the presence of noise, is equal to or better than the required threshold contrast, e.g., $c_0 = 5.0 \times 10^{-10}$ for milestone 1b.

Because of laboratory instabilities and the ongoing wavefront control algorithm, the contrast at any point in the dark field is time dependent, and so multiple successive exposures of the dark hole will be taken. For each image (where “each image” can itself be more than one sequential image if temporal averaging is deemed important to build up signal to noise), we calculate a spatial average of the measured contrast level over the entire dark hole. This yields a series of n (with $n \geq 4$) individual dark hole images, each with its own spatially-averaged dark hole contrast, c_i . We next take an average over the series of n dark hole images, leading to a sample-averaged contrast and variance, both defined below. To avoid confusion, we refer to spatial averages over an image region as “averages”, and averages of quantities over a number (sample) of images as “means”. Finally, we note that the entire experimental run is then to be repeated from scratch at least 3 times, to show repeatability. No averaging is done over the independent runs, so that the milestone is achieved independently m times.

As mentioned, the measured contrast is time dependent, being subject to laboratory conditions such as the quality of the optical components, their alignment, drifts in their alignment over time, and the effectiveness of each wavefront sensing and control cycle. With each iteration, the wavefront sensing and control procedure attempts to improve the contrast, thus compensating for any drift or alignment changes that may have occurred since the previous iteration. Further variations may be expected due to experimental noise and any limitations in the algorithm. The images built up from a sequence of such iterations will provide a distribution of contrast values, which will be regarded as Gaussian about a mean contrast for the data set. We therefore consider the mean contrast value as representative of the true contrast value for a given data set.

The contrast measurements of the iterations within a single run will fluctuate due to both random wavefront control errors and random measurement errors. The statistical confidence level will thus require an estimation of the variance. Given that our speckle fields contain a mix of static and quasi-static speckles (the residual light field remaining after the completion of a wavefront sensing and control cycle, together with the effects of alignment drift following the control cycle), as well as other sources of measurement noise including photon detection statistics and CCD read noise, an analytical development of speckle statistics is impractical. We will thus compute the confidence levels under the assumption of Gaussian statistics. (The full set of measurement will also be stored, to enable computation of the confidence levels for other statistics.)

The following paragraphs define the terms involved in the measurement process, spell out the measurement steps, and specify the data products.

5.1. Definitions

5.1.1. “Raw” Image and “Calibrated” Image. Standard techniques for the acquisition of CCD images are used. A “raw” image is the pixel-by-pixel image obtained by reading the charge from each pixel of the CCD, and amplifying and sending it to an analog-to-digital converter. A “calibrated” image is a raw image that has had background bias subtracted and the detector responsivity normalized by dividing by a flat-field image. (Saturated images are avoided in order to avoid the confusion of CCD blooming and other potential CCD nonlinearities.) A calibrated image can also include the step of low-order aberration contribution subtraction based on wavefront information provided by a low-order wavefront sensor, if one is available).

5.1.2. “Scratch” is a DM setting in which actuators are set to a predetermined surface figure that is approximately flat (typically, about 20 volts on each actuator).

5.1.3. The “algorithm” is the computer code that takes as input the measured speckle field images, and produces as output a voltage value to be applied to each element of the DM, with the goal of reducing the intensity of speckles.

5.1.4. The “star” is a small pinhole illuminated with laser or broadband light relayed via optical fiber from a source outside the chamber’s vacuum wall (e.g., a laser or a filtered super-continuum white light source). The “small” pinhole is to be unresolved by the optical system; e.g., a 5- μm diameter pinhole would be “small” and unresolved by the 80- μm FWHM Airy disk in an f/100 beam at 600 nm wavelength. This “star” is the only source of light in the optical path of the coronagraph. It is a stand-in for the star image that would have been formed by a telescope system.

5.1.5. The “contrast field” is a dimensionless map representing, for each detector pixel, the ratio of its value to the value of the peak of the PSF that would be measured in the same testbed conditions (light source, exposure time, Lyot stop, etc.) if the vortex mask were removed. The calibration of the contrast field is discussed in Section 5.3.

5.1.6. The “average contrast”, c_i , is a dimensionless quantity that is, for a given image, the spatial average value of the contrast field over the defined dark hole. Explicitly, an image’s average contrast is the sum of the contrast values for all pixels in the dark field, divided by the total number of pixels in the dark field, with no weighting applied.

5.1.7. The “mean contrast”, \hat{c} , of a given sequence of $n \geq 4$ images is the mean of the individual average contrast values occurring in that sequence:

$$\hat{c} = \frac{1}{n} \sum c_i.$$

5.1.8. “Milestone metric”: \hat{c} is the milestone metric.

5.1.9. “Standard Deviation”: The standard deviation σ_{meas} for an individual measurement of the average contrast value c_i of a sequence of contrast images given as usual by:

$$\sigma_{meas} = \sqrt{\frac{\sum_{i=1}^n (c_i - \hat{c})^2}{n - 1}}$$

The uncertainty in the mean contrast \hat{c} is then given by

$$\sigma_{mean} = \frac{\sigma_{meas}}{\sqrt{n}}.$$

There is also a contribution to the uncertainty from the independently-determined photometry error, σ_{phot} . The net standard deviation is thus

$$\sigma = \sqrt{\sigma_{mean}^2 + \sigma_{phot}^2}$$

5.1.10. “Statistical Confidence”. For contrast values that have a Gaussian distribution about the mean contrast, the statistical confidence that the mean contrast \hat{c} is less than some value c_0 is given by

$$conf(z < t) = \frac{1}{\sqrt{2\pi}} \int_{-\infty}^t e^{-z^2/2} dz = \frac{1}{2} + \frac{1}{\sqrt{2\pi}} \int_0^t e^{-z^2/2} dz$$

where $t = (c_0 - \hat{c})/\sigma$. Thus, as $\hat{c} = c_0 - t\sigma$, meeting a milestone contrast target c_0 with the desired confidence level requires the final measured mean contrast for a given run, \hat{c} , to be lower than the target contrast c_0 by t standard deviations. The Gaussian integral is widely tabulated, and $conf = 0.9$ implies $t = 1.28$. Thus, for 90% confidence, $\hat{c} = c_0 - 1.28\sigma$, i.e., the measured \hat{c} is smaller than the target c_0 by 1.28σ .

5.2. Measurement of the Star Brightness

5.2.1. The vortex mask is displaced laterally relative to the center of the beam by approximately $10 \lambda/D$ or so, so as to transmit maximum stellar flux.

5.2.2. To create the photometric reference, a representative sample of short-exposure (e.g. a few milliseconds) images of the star is taken, with all coronagraph elements other than focal-plane vortex mask in place.

5.2.3. The images are averaged to produce a single star image. The “short-exposure peak value” of the star’s intensity is estimated. Since the star image is well-sampled in the CCD focal plane (the Airy disk can be sampled by ~ 20 pixels within a radius equal to the full width half maximum), the star intensity can be estimated using either the value of the maximum-brightness pixel or an interpolated value representative of the apparent peak.

5.2.4. The “peak count rate” (counts/sec) is measured for exposure times of microseconds to tens of seconds.

5.3. Measurement of the Coronagraph Dark Hole Contrast Field

5.3.1. The vortex mask is centered on the star image.

5.3.2. An image with a typical exposure time of several seconds is taken of the coronagraph field (the suppressed star and surrounding speckle field). The target dark hole is a D-shaped field extending from 3 to $10\lambda/D$, bounded by a straight line passing $3\lambda/D$ from the star at its closest point, and by a circle of radius $10 \lambda / D$ centered on the star.

5.3.3. The image is normalized to the “star brightness” as defined in 5.2, using the fixed ratio between peak star brightness and the integrated light in a region of the speckle field outside the central DM-controlled area. I.e., dark-hole/star = dark-hole/speckle * speckle/star. For this purpose, any well-defined region of the outer speckle field can be used; the red region in Figure 26 (taken from TPF-C Milestone Report #1, Trauger et al. 2006) is only illustrative.

(In slightly more detail, to avoid saturation issues with the full-flux image case, there are usually three ratios involved: dark hole pixel/distant speckle field (both obtained with the vortex in); distant speckle field/inner point spread function [out to several Airy rings (about 200 pixels); both obtained with vortex out]; and inner point spread function/central point spread function pixel [both with vortex out]). In our previous TDEM work, we found the distant speckle field to be unchanged by the insertion or removal [by lateral translation] of the vortex, thus providing a robust calibration ladder. Other calibration ladders may also be possible.

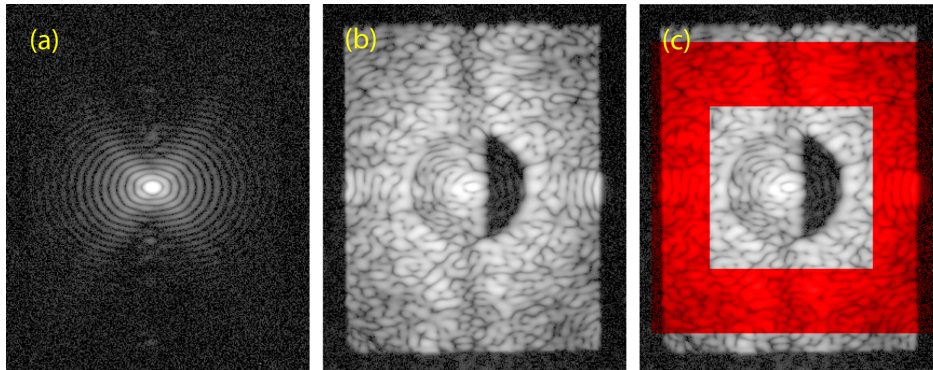


Figure 26. Reference field for contrast photometry. Shown here are (a) the “star” reference image, (b) the high-contrast coronagraph field; and (c) the same with a region of the reference speckle field in the “uncontrolled” area beyond the DM’s Nyquist limit superimposed in red. (Any subset of the red region can be used). Images are displayed with a logarithmic contrast stretch.

5.4. Milestone Demonstration Procedure

5.4.1. The DM is set to scratch. An initial coronagraph contrast field image is obtained as described in Sec. 5.3.

5.4.2. Wavefront sensing and control is performed to find settings of the DM actuators that give the required high-contrast in the target dark field. This iterative procedure may take from one to several hours, starting from scratch, if no prior information is available. However it can take more or less time depending on the stability of the optical system.

5.4.3. A number of contrast field images are taken, following steps 5.4.1 – 5.4.2. A sufficient number (≥ 4) of images are taken to provide statistical confidence that the milestone contrast levels have been achieved, as described in Section 5.1.

5.4.4. Laboratory data are archived for future reference, including all raw images of the reference star and contrast field images.

5.5. Milestone Data Package

The milestone certification data package will contain the following:

5.5.1. A narrative report that includes a discussion of how each element of the milestone was met, with a narrative summary of the overall milestone achievement and its repeatability.

5.5.2. A description of the optical elements, including the vortex masks, and their significant characteristics.

5.5.3. A tabulation of the significant operating parameters of the apparatus.

5.5.4.a A representative contrast field image from the set of images used in the statistical analysis of the milestone, with appropriate numerical contrast values indicated, with coordinate scales indicated in units of Airy distance (λ/D).

5.5.4.b The mean contrast field image for the set of images used in the statistical analysis of the milestone, with appropriate numerical contrast values indicated, with coordinate scales indicated in units of Airy distance (λ/D).

5.5.5. A description of the data reduction algorithms, in sufficient detail to guide an independent analysis of the delivered data.

5.5.6. Average and mean contrast values and standard deviations for the data used to satisfy the milestone requirements, including a pixel-by-pixel histogram of contrast values across the dark field.

5.5.7. For each image reported as part of the milestone demonstration, the average contrast within the area spanning 3-4 λ/D .

6. Success Criteria

The following are the required elements of the milestone demonstration. Each element includes a brief rationale.

6.1. Illumination is single or dual polarization at a wavelength in the range of 300 nm $< \lambda < 1000$ nm, for 0% or 10% bandwidth, depending on the specific milestone.

Rationale: *This milestone is an initial demonstration of the feasibility of the approach at a wavelength in the science band of Exo-C/Habex/LUVOIR.*

6.2. The contrast specified in each milestone in Section 3 shall be achieved in a 3 to 10 λ/D dark zone, using the basic geometry of Fig. 9, but with the OWA at 10 λ/D .

Rationale: *This provides evidence that the high contrast field is sufficiently dark to be useful for searching planets, yet within proven testbed performance capabilities.*

6.3. Criterion 6.2 shall be met with a confidence of 90% or better. Sufficient data must be taken to justify this statistical confidence.

Rationale: *Assuming the contrasts have a Gaussian distribution about the mean, this demonstrates a statistical confidence of 90% that the contrast goal has been met.*

6.4. Elements 6.1 – 6.3 must be satisfied on 3 separate occasions with a reset of the wavefront control system software (DM set to scratch) between each demonstration.

Rationale: *This provides evidence of the repeatability of the contrast demonstration.*

The wavefront control system software reset between experimental runs ensures that the different data sets can be considered as independent and do not represent an unusually good configuration that cannot be readily reproduced. For each demonstration, the DM will begin from a "scratch" setting. There is no time requirement for the demonstrations, other than the time required to meet the statistics stipulated in the success criteria. There is no required interval between demonstrations; subsequent demonstrations can begin as soon as prior demonstrations have ended. There is also no requirement to turn off power, open the vacuum tank, or delete data relevant for the calibration of the DM influence function.

7. Schedule

As described in our selected TDEM17 proposal and Fig. 28 here, our approved TDEM test plan has a duration of three years. In short, we plan to use both the HCST and the DST during the first two years, and then concentrate our work in the DST in the third year.

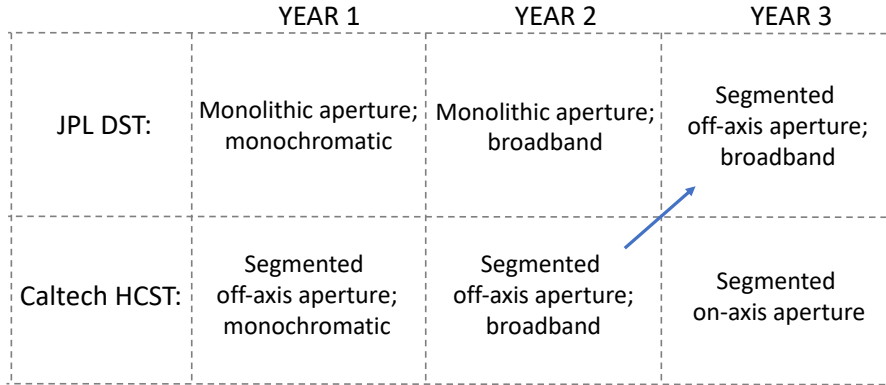


Figure 28. *Overall testbed project schedule.*

The Caltech HCST is under the control of the PI, Dimitri Mawet, and is available to be used as indicated in Fig. 28, from now until the transition of the segmented aperture work to the DST roughly two years down the road. After that, it will be used for on-axis segmented aperture tests.

In the JPL DST, we plan to carry out vortex testing work at a duty cycle of roughly one-third time over the course of our 3-year program. Our DST work plan consists of six six-month cycles, with each individual cycle consisting of four months of preparatory work outside of the DST chamber (allowing for, e.g., purchasing of improved vortex masks and other optics) followed by two months of in-chamber testing time. Due to other already planned work in the DST, the DST will not be available for our first TDEM17 vortex run until sometime in 2020, at which point the first of our six DST testing runs would commence.

The baseline plan for our six DST runs is as follows: the first two runs are aimed predominantly at monochromatic contrast testing, the next two at broadband contrast testing (all four for monolithic aperture work), and the next two for segmented aperture work. Of course, it may well be possible to combine work toward different milestones for greater efficiency, and we will take advantage of such synergies whenever possible. In addition, depending on how rapidly the segmented-aperture and monolithic-aperture work progress, those two testing sequences could be interleaved somewhat, if that would enable more rapid progress in either or both of these areas.

Finally, we note that the JPL facility team will be responsible for all DST assembly and alignment steps, for all control and dark-hole generation software, and for any upgrades to the DST facility. As a result, the facility team will likely need additional DST time outside of our official TDEM test runs for such work. We will, however, be happy to work with the DST team to mesh our respective tasks in order to optimize the facility schedule.

8. References

- Absil, O. et al., “Three years of harvest with the vector vortex coronagraph in the thermal infrared,” SPIE 9908, 99080Q, 2016.
- Bottom M. et al., “Stellar double coronagraph: a multi-stage coronagraphic platform at Palomar Observatory,” PASP 128, 075003, 2016.
- Fogarty, K. et al., “Polynomial apodizers for vector vortex coronagraphs,” AJ 154, art. id. 240, 2017.
- Foo, G., Palacios, D. M. and Swartzlander, Jr., G. A., “Optical Vortex Coronagraph,” Opt. Lett. 30, 3308, 2005.
- Give’on, A. et al., “Broadband wavefront correction algorithm for high-contrast imaging systems,” Proc. SPIE 6691, 66910A, 2007.
- Give’on, A., “A unified formalism for high contrast imaging correction algorithms,” Proc. SPIE 7440, 74400D, 2009.
- Komanduri, R. K. et al., “Multi-twist retarders for broadband polarization transformation,” Proc. SPIE 8279, 82790E (2012).
- Marrucci, L., Manzo, C. & Paparo, D. “Optical Spin-to-Orbital Angular Momentum Conversion in Inhomogeneous Anisotropic Media,” Phys.Rev.Let. 96, 163905 (2006).
- Mawet, D., Riaud, P., Absil, O. and Surdej, J., “Annular Groove Phase Mask Coronagraph” ApJ, 633, 1191, 2005.
- Mawet, D. et al., “Optical Vectorial Vortex Coronagraphs using Liquid Crystal Polymers: Theory, Manufacturing and Laboratory Demonstration,” Opt. Exp., 17, 1902, 2009.
- Mawet, D. et al., “Taking the vector vortex coronagraph to the next level for ground- and space-based exoplanet imaging instruments: review of technology developments in the USA, Japan, and Europe,” Proc. SPIE 8151, 815108-1, 2011.
- Mawet, D. et al., “Ring-apodized Vortex Coronagraphs for Obscured Telescopes. I. Transmissive Ring Apodizers,” ApJ Suppl. 209, 7, 2013.
- Murakami, J. et al., “Coronagraph focal-plane phase masks based on photonic crystal technology: recent progress and observational strategy,” Proc SPIE 8442, 844205, 2012.
- Pancharatnam, S., “Achromatic combination of birefringent waveplates,” Proc. Indian Acad. Sci. A 41, 137, 1955.
- Roberts, D. et al., “Overcoming the tradeoff between efficiency and bandwidth for vector vortex waveplates,” Proc. 2019 IEEE Aerospace Conf., 2019.
- Ruane, G. et al., “Apodized vortex designs for segmented aperture telescopes,” Proc. SPIE 9912, 99122L 2016
- Ruane et al., “Performance and sensitivity of vortex coronagraphs on segmented space telescopes” Proc. SPIE 10400, 104000J, 2017
- Ruane, G. et al., “Vortex coronagraphs for Habitable Exoplanet Imaging Mission Concept: theoretical performance and telescope requirements,” JATIS 4, 015004, 2018

Ruane, G. et al., “Decadal Survey Testbed Commissioning Roadmap: Demonstrating Technology for Imaging New Worlds,” 2019

https://exoplanets.nasa.gov/internal_resources/1170/

Serabyn, E. et al., “High-contrast imaging results with the vortex coronagraph,” Proc. SPIE 8864, 88640Y (2013).

Serabyn, E., et al., “Vector vortex coronagraphy for exoplanet detection with spatially variant diffractive waveplates,” JOSA B 36, D13

Swartzlander, G., “The optical vortex coronagraph,” J. Opt. A., 11, 1464, 2009.

Trauger, J. et al., “TPF-C Milestone #1 Report,” JPL Document D-35484, 2006.

Trauger, J. et al., “ACCESS – A Concept Study for the Direct Imaging and Spectroscopy of Exoplanetary Systems,” in “Pathways towards Habitable Planets,” ASP Conf. Series 430, 375, 2010.

Zhang, M. et al., “Characterization of microdot apodizers for imaging exoplanets with next-generation space TELESCOPES SPIE 10698, 106985X, 2018